Near-Infrared Band Strengths of Molecules Diluted in N_2 and H_2O Ice Mixtures Relevant to Interstellar and Planetary Ices

C. R. Richey[1] and P. A. Gerakines[2]

Astro- and Solar-System Physics Program, Department of Physics, the University of Alabama at Birmingham, Birmingham, AL 35294-1170

christina.r.richey@nasa.gov, gerak@uab.edu

Corresponding Author: Christina R. Richey

(205)746-9591, Fax: (301)286-1617

ABSTRACT

In order to determine the column density of a component of an ice from its infrared absorption features, the strengths of these features must be known. The peak positions, widths, profiles, and strengths of a certain ice component's infrared absorption features are affected be the overall composition of the ice. Many satellites within the solar system have surfaces that are dominated by H_2O or N_2 and ices in the interstellar medium (ISM) are primarily composed of H_2O. The experiments presented here focus on the near -infrared absorption features of CO, CO_2, CH_4, and NH_3 (ν=10,000-4,000 cm^{-1} , λ=1-2.5 μm) and the effects of diluting these molecules in N_2 or H_2O ice (mixture ratio of 5:1). This is a continuation of previous results published by our research group.

Subject headings: Ices: IR spectroscopy – Satellites: general – Satellites: surfaces – Spectroscopy

1. Introduction

A variety of frozen volatile species ("ices") are observed in the mantles coating the dust grains of the dense interstellar medium (ISM), where they are dominated by H_2O or N_2 (e.g.,

[1]present address: NASA GSFC, Mail Code 665, Greenbelt, MD, 20771

[2]present address: Astrochemistry Laboratory, NASA GSFC, Greenbelt, MD, 20771

Gibb et al. 2004), and on the surfaces of planetary bodies in the outer Solar System (e.g., Roush 2001). Since the spectral properties (peak positions, spectral profile structures, and absorption strengths) of most species may be significantly altered by dilution, it is important to study them in an appropriate ice matrix. Here, we extend our previous study of the near-infrared spectral properties of pure ices (Gerakines et al. 2005) to those of molecules present within H_2O- and N_2-dominated ice mixtures.

The compositions of interstellar icy grain mantles are dominated by H_2O, by about a factor of 2 over the next-most abundant ice species, with minor components dependent upon the specific environment probed along a chosen line of sight. Some of the most significant minor components of interstellar ices include CO (1-10% relative to H_2O), CO_2 (10-30 %), CH_4 (1-5 %), and NH_3 (~1 %; with some dependence on the environment sampled in the observed line of sight (e.g., Gibb et al. 2004). Moreover, infrared spectroscopy of the vibrational absorption features of these minor components indicates that while H_2O-poor ice components do exist, a significant majority of icy mantle species appear to be diluted within an H_2O-ice matrix (e.g., Tielens et al. 1991; Chiar et al. 1995; Boogert et al. 1996; Gerakines et al. 1999; Oliveira et al. 2009).

In the outer solar system, many cold planetary surfaces appear or are thought to be dominated by H_2O (see, e.g., Hudson & Moore 2001), such as those of cometary nuclei (Roush 2001; Gibb et al. 2003), some Galilean satellites (e.g., McCord et al. 1998; Hibbitts et al. 2000; Hansen & McCord 2008), many of the Saturnian satellites (e.g., Filacchione et al. 2007; Lopes et al. 2008), and many Kuiper Belt Objects (Jewitt & Luu 2004; Trujillo et al. 2005). Spectral modeling of the reflectance spectra indicate trace species on these surfaces such as CH_4, CO_2, and NH_3 (e.g., Hibbitts et al. 2003; Cruikshank 2007; Schaller & Brown 2007; Clark et al. 2008). Molecules diluted in N_2 have been identified on planetary bodies such as Pluto and Triton (e.g., Cruikshank et al. 1998; Quirico et al. 1999; Buie & Grundy 2000; Grundy et al. 2003) and N_2 and CH_4 have been detected on large Kuiper Belt Objects (KBOs) such as Sedna (K130) (Barucci et al. 2005) and Eris (Brown 2008).

By and large, the current state of knowledge about the composition of interstellar ices comes from observations and laboratory simulations of spectra obtained at mid-IR wavelengths ($\lambda = 2.5 - 25\,\mu$m). This is due to the fact that the strongest absorption features of most small molecules in the solid phase fall in the mid-IR spectral region. These features are usually caused by fundamental molecular vibrational modes and are therefore the most sensitive tracers of ice composition (e.g., the 3.05 μm O-H stretching vibration feature of H_2O or the 4.26 μm C=O stretching vibration feature of CO_2).

In contrast, the majority of what is known about Solar System ices has been obtained from the spectra of reflected sunlight in the near-IR spectral region, where the absorption

features due to overtones and combinations of the molecular vibrational modes are found. These features are weaker than the fundamental modes (e.g., Gerakines et al. 2005), but there is a higher flux of solar radiation in the near-IR. Most work in literature uses the wavelengths of absorption features in pure, unprocessed ices in comparison to observed data in order to deduce the general composition of icy surfaces (e.g., Roush 2001), however recent experiments use ice mixtures (e.g., H_2O+NH_3 by Moore et al. 2007 and N_2+CH_4 by Brunetto et al. 2008). There is a need for laboratory mixtures in order to make accurate comparisons due to the fact that mathematical addition of individual spectra does not take into account the interactions of ice components when present in an intimate mixture.

Studies of interstellar ices have extended into the near-IR spectral region as well. An example includes observations made with SpeX on the Infrared Telescope Facility (IRTF) telescope (Vacca et al. 2004). The James Webb Space Telescope (JWST) Near Infrared Spectrometer (NIRSpec) will perform observations from 0.6 to 5 μm at spectral resolutions from 100 to 3000 (Rauscher et al. 2004), and will call for an increase in near-IR data. With our data, calculations of ice abundances in star-forming regions could be accomplished.

A vital aspect of understanding ices on cryogenic surfaces in the ISM is the accurate determination of the abundances of the ice components. This relies on accurate laboratory measurements of physical parameters called band strengths. For example, the column density of a molecule in the solid phase (N, in units of cm^{-2}) as determined from astronomical observations of transmitted starlight is commonly calculated from the optical depth spectrum $\tau(\tilde{\nu})$ using the formula

$$N = \frac{\int_i \tau(\tilde{\nu})\, d\tilde{\nu}}{A_i}, \tag{1}$$

where the A_i is the band strength of molecular absorption feature i (in units of cm molecule^{-1}), and the integration is taken over the wavenumber range of feature i.

From Equation (1) it is clear that the accuracy of the compositional information that may be derived from the astronomical data $\tau(\tilde{\nu})$ is closely tied to the accuracy of the band strength A_i. Additionally, one cannot, in general, apply the same band strength to all ice mixtures containing the same molecular absorption feature, but it must be determined for each mixture individually as this parameter is dependent upon the specific physical conditions of the local molecular environment (neighboring molecules, crystalline structure, temperature, etc.; see, e.g., Gerakines et al. 1995 or Quirico & Schmitt 1997). The determination of surface ice composition from a reflectance measurement also depends on the strengths of ice absorption features (or more precisely, the optical constants of the ice), as these parameters are required as input to surface scattering models used for interpretation.

The IR absorption features of most molecules of astrophysical interest have band strengths

from about 10^{-20} to 10^{-16} cm molecule^{-1}, where the strongest absorption features generally lie in the mid-IR. Our laboratory group has already published a study of the near-IR band strengths of pure CO, CO_2, C_3O_2, H_2O, NH_3, CH_4, and CH_3OH ice films at low temperature (Gerakines et al. 2005). This is a continuation of that work, using the same techniques, to the near-IR band strengths of selected mixed ices. Following the methods of Gerakines et al. (2005), here we present the near-IR band strengths of CO, CO_2, CH_4, and NH_3 as diluted in either N_2 or H_2O, in the mixing ratio of ~5:1 at a temperature of 5 K.

2. Experimental Methods

The experimental setup and ice creation techniques are identical to those described by Gerakines et al. (2005) and similar to those in previous studies by, e.g., Hudgins et al. (1993) or Gerakines et al. (1995). To summarize, the sample gases were deposited onto an IR-transparent substrate (CsI) at low temperature (~ 5 K) inside a high-vacuum sample chamber, and the resulting films were analyzed by FTIR spectroscopy. The vacuum system pressure was approximately 3×10^6 torr at room temperature before cooling the substrate. The substrate is attached to the end of a rotatable cold finger that may be cooled by a closed-cycle helium refrigerator (Air Products Displex 202N system). The temperature is continuously monitored by a chromel-Au thermocouple and is adjustable by a resistive heater element from 5 K up to room temperature.

The gases to be studied are mixed in the desired mixing ratio in a gas bulb attached to a separate manifold then transferred to the high-vacuum system. The sample gases are released within the vacuum chamber at a position about 1 cm in front of the substrate. Gas flow into the system is controlled by a needle valve, and flow rates are adjusted by this valve to achieve film growth rates of about 1-5 μm hr^{-1}. Two of the external ports of the vacuum chamber hold IR transparent windows made of KBr, and the entire chamber is situated inside the sample compartment of a ThermoMattson Infinity Gold FTIR spectrometer such that the IR beam passes at normal incidence through the KBr external ports and the CsI substrate.

The spectrometer optics is capable of automatic switching between the configurations of sources, detectors, and beamsplitters without breaking the dry air purge, allowing for the measurement of both near-IR spectra over the range of 10,000 to 3500 cm^{-1} (1.0 to 2.86 μm) and mid-IR spectra from 4,500 to 400 cm^{-1} (2.22 to 25.0 μm). All spectra in this study were taken at a resolution of 4 cm^{-1}, which is suitable due to previous studies indicating the FWHM of these features was larger than 4 cm^{-1} (Gerakines et al. 2005). Ice samples created by vacuum deposition at ~5 K are expected to be amorphous rather than crystalline, and

this was supported by the absorption profiles in the resulting IR spectra. The gases used and their purities are as follows: N_2 (Matheson, 98+%), CO (Matheson, 99.9%), CO_2 (Matheson, 99.8%), CH_4 (Matheson, 99+%), NH_3 (Matheson, 99+%), and H_2O (distilled by freeze-thaw cycles under vacuum).

By assuming a linear baseline, the integrated absorbance of each feature (in units of cm^{-1}) was measured and the errors in the feature areas were estimated by integrating across the same limits when no feature was apparent above the noise level in the infrared spectrum. For narrow features ($\Delta\tilde{\nu} \lesssim 10\,cm^{-1}$), the errors were found to be about 0.006–0.01 cm^{-1}. This varied in direct proportion to a feature's width.

For a given molecule, the relative strengths of two absorption features were determined from the relationship between the areas of these bands as the ice was grown. While one could use a single ice spectrum and determine the relative strengths of any two features by taking the ratio of their areas, since the near-IR features are much weaker than those in the mid-IR (~10-100 times smaller; see absorbance scales in Fig. 1 and Fig. 2), errors in their measured areas are relatively much higher. Systematic errors involved in measuring the areas of the near-IR features are significantly reduced by monitoring the relationship between two given absorption features over the course of a slow deposit.

In the experiments presented in the next section, we created mixtures of CO, CO_2, CH_4, and NH_3 diluted in N_2 and diluted in H_2O with approximate compositions of dilutant:sample of 5:1. These mixtures were chosen in order to represent some of the most general cases in both the ISM or the outer Solar System. Dilution in H_2O is meant to represent the environment of interstellar icy grain mantles or icy moons, such as Europa or Enceladus (Brown 2006, Hansen & McCord 2008). Dilution in N_2 is meant to represent the environment of icy moons dominated by N_2, such as Triton (Buie & Grundy 2000, Stansberry 2004). Mixture ratios were not meant as a literal representation of astrophysical bodies, rather, mixtures were meant to be dilute enough to simulate a N_2- or H_2O-dominated environment.

For each sample molecule, the selected mixture was prepared in the gas manifold as described above. After cooling the substrate to $\sim 5\,K$, the gases were slowly bled into the vacuum system and the ice film was allowed to grow continuously over the course of several hours to days. The film growth was monitored at regular intervals, taking both near- and mid-IR spectra throughout the growth period. At each stage, the integrated areas of the mid- and near-IR features were measured. When it was determined that most of the near-IR absorption features were of sufficient strength to establish a clear trend, the gas flow was stopped and the experiment was ended. For each mixture involving H_2O, it was necessary to replenish the gas bulb during the growth in order to deposit a sufficiently thick sample.

3. Results

The spectra of ices containing solid CO, CO_2, CH_4, and NH_3 diluted in N_2 in a ~5:1 mixture ratio and of ices containing solid CO, CO_2, CH_4, and NH_3 diluted in H_2O in a ~5:1 mixture ratio were collected in the near-IR region from 10,000 to 3,500 cm^{-1} (1.0-2.9 μm) and the mid-IR region from 4,500 to 400 cm^{-1} (2.2-25 μm) during the slow growth of films at ~5 K. Figure 1 displays the spectra of the N_2-dominated samples and Figure 2 displays the spectra of the H_2O-dominated samples. If possible, the band strengths of any near-IR absorption features observed in the spectra were determined using the method described below.

For optically thin ice absorptions, depositing a certain number of molecules should cause a linear increase the areas under all absorption features, where the rate of increase in area versus column density is equal to that feature's band strength– see Eq. (1). Hence, for a given molecule, the trend in one particular feature's integrated area versus that of another feature of the same molecule should initially be a straight line whose slope corresponds to the ratio of the band strengths of the chosen features. In our case, we have chosen to compare the integrated areas of the observed near-IR features of each of the molecules under study to the areas of their much stronger mid-IR features. The mid-IR features used for these comparisons and their previously determined band strengths are listed in Table 1. Figures 3 - 6 display the near-IR regions of the spectra where absorptions were observed as well as the plots of the near-IR feature areas versus mid-IR feature areas for the N_2-dominated ice mixtures. Figures 7 - 10 display the corresponding spectra and band area plots for the H_2O-dominated ice mixtures. For peaks where there is an underlining feature of H_2O (see Figure 8 for example), we drew a linear baseline underneath the feature to remove the underlying absorption due to H_2O.

Once the slope of the linear trend in the near-IR area versus mid-IR area is determined, it may be multiplied by the known band strength of the mid-IR feature (from Table 1) to obtain the near-IR band strength. Mid-IR band strength data exist for mixtures similar to the H_2O-ice mixtures and the N_2+ CH_4 mixture studied here (Brunetto et al. 2008; Kerkhof et al. 1999; Gerakines et al. 1995) and those results were used to determine our near-IR band strength values. For CO, CO_2, and NH_3 in N_2-dominated mixtures, no such studies have been reported in the mid-IR. However, the studies of the molecules in H_2O have shown that the mid-IR band strengths change by less than 20% relative to their pure-ice values (e.g. Gerakines et al. 1995). Since N_2 is a non-polar molecule, it can be expected that its effects would be even less pronounced. This is consistent with data for CH_4 (Kerkhof et al. 1999; Brunetto et al. 2008). Hence, where data for N_2-dominated mixtures are unavailable, we have used the mid-IR band strengths for pure ices, with the caveat that this may introduce an error

of approximately 20% (but this is within the typical error in our measurements; see results below). Observed feature parameters (positions, widths, and vibrational assignments), slopes obtained for the linear trends in the near-IR vs. mid-IR areas, and calculated band strengths using this method are given in Table 2 for N_2-dominated mixtures and in Table 3 for H_2O-dominated mixtures. The listed uncertainties in near-IR band strengths were obtained by multiplying the standard deviations in the best-fitting slopes by the mid-IR band strengths and do not include the systematic errors associated with the band strength used for scaling.

For some of the molecules (CO, CO_2, and CH_4), the scaling process was complicated by the fact that some mid-IR absorptions became saturated (with peak absorbance values greater than 1.0) early in the ice film growth. The curves of growth were highly non-linear. Thus, weaker features needed to be used in order to produce linear trends. For the CO ice deposits the absorption feature of ^{13}CO at 2092 cm^{-1} (4.780 μm) was used to scale the ^{12}CO and ^{13}CO near-IR features. The strength of 1.5×10^{-19} cm per ^{12}CO molecule was used for the 2092 cm^{-1} (4.780 μm) feature, taking the band strength of the ^{13}CO feature from Gerakines et al. (1995) and scaling by the terrestrial ratio of $^{12}C/^{13}C$ of 87. For N_2 + CO_2 (5:1), the combination mode at 3711 cm^{-1} (2.695 μm) was used. For the H_2O + CO_2 (5:1) ice deposit, the 2280 cm^{-1} feature of $^{13}CO_2$ was used in the same manner. For the H_2O + CH_4 (5:1) ice the mid-IR absorption feature at 1306 cm^{-1} (7.657 μm) was used for scaling (strengths are listed in Table 1).

In the N_2 + CH_4 ice, the feature due to the CH_4, the $\nu_2+\nu_4$ vibration mode at 2825 cm^{-1} (3.540 μm), was used, assuming a band strength of $A = 2.8\times10^{-19}$ cm $molecule^{-1}$ (corresponding to the 2815 cm^{-1} feature in pure CH_4 ice as determined by Brunetto et al. 2008). Note, in Gerakines et al. 2005, a scaling error caused each of the pure CH_4 results to be off by a factor of 7 and was corrected for future work.

A small level of contamination due to CO_2 ($\sim$2 %, as determined from the size of the absorption) was also observed within the N_2 ice mixtures, as is seen in Figure 1. Additionally, a very small amount of H_2O was seen in the N_2 ice mixture ($\lesssim$ 1 %). The value is small enough to not be seen in the Figure 1, due to the short time scale required for N_2-dominated mixtures versus the H_2O-dominated mixtures, which required changing of gas bulbs and additional pumping time between scans (as described in the Experimental Methods Section). Near-IR features occurring at $\sim$7300 cm^{-1} and $\sim$5200 cm^{-1} were observed in many H_2O-dominated spectra (e.g., in Figure 2). These features were determined to be caused by small amounts of CO_2 and N_2 contamination within the H_2O used to create the gas mixtures. This was not expected to significantly affect the band strength results.

4. Comparisons with previous studies

In this section, we compare these results to those found in the study of pure ices by Gerakines et al. (2005), and to other works in the literature.

4.1. N_2 + CH_4

For CH_4 diluted in N_2, no visible features were detected for the $(\nu_2 + 2\nu_3 + \nu_4)$ and $3\nu_3$ vibrational modes near 8780 and 9060 cm^{-1}, however this may have been due to noise in the spectrum. All other vibrational modes showed an increase in peak wavenumber relative to pure CH_4 (ranging from 10 cm^{-1} to 23 cm^{-1} respectively). All of the features were broader than in pure CH_4 (by 2 cm^{-1} to 11 cm^{-1}), with the exception of the $(\nu_1 + \nu_4)$ mode, which saw no broadening or sharpening of the peak, and the $[\nu_1]+[\nu_1]+[\nu_4]+[\nu_4]$ and the $(2\nu_3+2\nu_4)$ modes, which saw sharpening of the peaks and a decrease in the FWHM by 4 cm^{-1} and 7 cm^{-1} respectively. Band strengths for the $(\nu_3+\nu_4)$, $(\nu_2+\nu_3)$, $2\nu_3$, and $(\nu_2+2\nu_3)$ features (at 4311, 4539, 6000, and 7503 cm^{-1} respectively) measured were lower than those in the pure ice by a factor of $3-13$. The $(\nu_2 + \nu_4)$, $(\nu_1 + \nu_4)$, $(\nu_3 + 2\nu_4)$, and $(\nu_2 + \nu_3 + \nu_4)$ features (at 4125, 4222, 5576, and 5811 cm^{-1} respectively) saw little to no change in the band strengths in comparison to the pure ice (< 10 %). Due to the non-linear behavior of the growth curve at short deposition times, the strength of the $[\nu_1] + [\nu_1] + [\nu_4] + [\nu_4]$ feature at 8422 cm^{-1} could not be determined with accuracy.

Near-IR spectra of N_2 + CH_4 in (1:1) and (10:1) ratios were reported by Brunetto et al. (2008), and our band strengths are comparable. For all features, our 5:1 mixtures indicated slightly larger peak shifts relative to the pure ice of an additional $3-14$ cm^{-1}.

4.2. N_2+ CO_2

For CO_2 diluted in N_2, all expected near-IR vibrational modes were observed and showed a positive in peak position relative to the pure CO_2 ranging from 3 cm^{-1} to 11 cm^{-1}, with the exception of the $(2\nu_1 + 2\nu_2 + \nu_3)$ mode and the $3\nu_3$ mode, which showed a decreases in position of 1 and 2 cm^{-1} respectively. A slight broadening relative to pure CO_2 occurred in most features, ranging from 1 to 2 cm^{-1}, with the exception of the $(\nu_1 + 2\nu_2 + \nu_3)$ and $(2\nu_1 + \nu_3)$ modes, which showed no broadening or sharpening, and the $(4\nu_3 + \nu_2)$ feature, which showed a sharpening by 6 cm^{-1}. All measurable band strengths showed an increase by 1.3 to 2 times those of pure CO_2. Only small broadening and shifting occurred due to the nature of the apolar ices in the mixture (CO_2 and other apolar ices are not typically self-

interactive). The increase in band strength may have been due to the slight contamination mentioned in Section 3.

4.3. N_2 + CO

For CO diluted in N_2, all expected near-IR vibrational modes were observed and showed little change in peak position relative to pure CO (+1 cm^{-1} for all modes, except the $2\nu^{13}CO$, which showed no change in position). Broadening relative to pure CO occurred in each feature ranging between 1 and 5 cm^{-1}. The only measurable band strength was that of the 2ν ^{12}CO vibrational mode. The band strength was very comparable to the pure ice feature's band strength $(1.1 \pm 0.1) \times 10^{-19}$ cm $molec^{-1}$ versus $(1.6 \pm 0.1) \times 10^{-19}$ cm $molec^{-1}$ for the pure ice). As was seen with CO_2, CO saw only minimal broadening and shifts and almost no change in the band strength due to the nature of two apolar ices in mixture, indicating almost no change in the interaction of the molecules.

4.4. N_2 + NH_3

For NH_3 diluted in N_2, all expected near-IR vibrational modes were observed, with large shifts in the peak positions relative to pure NH_3. Decreases in position occurred in both the $(\nu_1 + \nu_2 + \nu_4)$ and the $(\nu_1 + \nu_2)$ modes (of 65 and 30 cm^{-1} respectively), while increases were seen in the peak positions of the $2\nu_1$ and $(\nu_1 + \nu_4)$ features (of 83 and 49 cm^{-1}). All features showed a sharpening of peaks relative to pure NH_3 with decreases of 55 cm^{-1} to 97 cm^{-1}. There was a decrease in the band strengths for the $(\nu_1 + \nu_2)$ and $(\nu_1 + \nu_4)$ features by a factor of 2 to 4 in comparison to those of pure NH_3 and an increase in the strength of the $2\nu_1$ mode feature by a factor of 2. When diluted with N_2, the mixture has fewer NH_3 - NH_3 interactions, likely resulting in the sharpening of the peaks.

4.5. H_2O + CH_4

For CH_4 diluted in H_2O, no visible absorption features were detected for the $(\nu_2 + 2\nu_4)$ vibrational mode near 4115 cm^{-1}. All other vibrational modes showed an increase in peak wavenumber relative to pure CH_4 (ranging from 4 to 213 cm^{-1} respectively), with the exception of the $(\nu_2 + \nu_3)$ and $3\nu_3$ modes at 4528 and 9039 cm^{-1} (the peak position of the $3\nu_3$ mode decreased by 21 cm^{-1} from the pure ice value). Most of the CH_4 absorption features in the H_2O mixtures were broader than their corresponding pure-ice values, with

increases in FWHM from 1 to 19 cm^{-1}, with the exception of the $[\nu_1] + [\nu_1] + [\nu_4] + [\nu_4]$, $(2\nu_3 + 2\nu_4)$, and $3\nu_3$ modes (at 8569, 8612, and 9039 cm^{-1}), which all showed a sharpening of the features with respect to their pure-ice values by $6 - 35$ cm^{-1}. Due to the non-linear behavior of the growth curves even at short deposition times, the strengths of only two near-IR features could be determined with accuracy, as listed in Table 3, and each were found to be weaker than in the pure ice.

A $H_2O + CH_4$ mixture was studied at 15 K in two dilution ratios (20:1 and 3:1) by Bernstein et al. (2006) from 1.5 to 25 μm (6700 to 400 cm^{-1}). Generally, our measured widths and band strengths agree with those reported for the $(\nu_1 + \nu_4)$, $(\nu_3 + \nu_4)$, $(\nu_2 + \nu_3)$, $(\nu_2 + \nu_3 + \nu_4)$, and $2\nu_3$ modes. For all features, our 5:1 mixtures displayed slightly higher peak shifts than Bernstein et al. (2006) relative to the pure ice of an additional $4 - 10$ cm^{-1}.

Gálvez et al. (2009) also studied several mixtures of $H_2O + CH_4$ at 14 K. We find that our results agree in widths and band strengths for their $H_2O + CH_4$(10:1) and (4:1) ice mixtures for the $(\nu_1 + \nu_4)$ and $(\nu_3 + \nu_4)$ modes. Peak positions were also similar, with only a differences of $5 - 8$ cm^{-1}.

4.6. $H_2O + CO_2$

For CO_2 diluted in H_2O, no visible features were detected for the $(4\nu_2+\nu_3)$ and $(4\nu_3+\nu_2)$ vibrational modes near 4840 and 9955 cm^{-1}. The $(\nu_1+2\nu_2+\nu_3)$ at 4965 cm^{-1}, decreased its peak positions by 6 cm^{-1} respectively in comparison to pure CO_2 value, while the $(2\nu_1+\nu_3)$ mode at 5087 cm^{-1} saw a slight decrease in position by 1 cm^{-1}. Larger shifts were seen for the $(\nu_1+4\nu_2+\nu_3)$ mode at 6051 cm^{-1} (decrease of 163 cm^{-1}), the $(2\nu_1+2\nu_2+\nu_3)$ mode at 6325 cm^{-1} (decrease of 16 cm^{-1}), and the $3\nu_3$ mode at 6864 cm^{-1} (decrease of 108 cm^{-1}). While broadening occurred in every peak, the most prominent peaks saw the least amount of increase in FWHM. The $(\nu_1+2\nu_2+\nu_3)$ and $(2\nu_1+\nu_3)$ modes at 4965 and 5086 cm^{-1} saw broadening of only 2 and 3 cm^{-1} respectively, while the $(\nu_1+4\nu_2+\nu_3)$, $(2\nu_1+2\nu_2+\nu_3)$, and $3\nu_3$ modes at 6051, 6325, and 6864 cm^{-1} saw much larger increases in FWHM (93, 71, and 171 cm^{-1} respectively). The strengths of only two absorption features could be determined with confidence: the $(\nu_1+2\nu_2+\nu_3)$ and $(2\nu_1+2\nu_2+\nu_3)$ modes, which showed a strength of $2 - 4$ times those of the pure CO_2 band strengths.

$H_2O + CO_2$ was also studied by Bernstein et al. (2005) at 15 K in two mixtures, 25:1 and 5:1, from 2 to 25 μm ($5000-400$ cm^{-1}). Several near-IR bands were detected, including the $(\nu_1+2\nu_2+\nu_3)$ feature, which in the 5:1 mixture showed a lower band strength 3.4×10^{-20} cm molecule^{-1} compared to our value of $(2.3\pm0.1)\times10^{-19}$ cm molecule^{-1}and a larger FWHM

(15 cm^{-1} compared to 9 cm^{-1}) than in our results. In the 25:1 mixture of Bernstein et al. (2005), the band strength and FWHM of this feature was consistent with those in our 5:1 mixture. In each case, we measured slightly different peak positions. The $(2\nu_1 + \nu_3)$ mode was not detected by Bernstein et al. (2005) in their 25:1 mixture; however, the properties of this feature in the 5:1 mixture were similar to those measured here. Bernstein et al. (2005) also observed two additional peaks, the $2\nu_3$ and $4\nu_2 + \nu_3$ modes, that were not visible in our spectra. This is likely due to overlapping H_2O features (see Figure 2 or Figure 8). Another reason for this may be that the $2\nu_3$ mode is a forbidden overtone of CO_2 and is extremely sensitive to conditions such as concentration and temperature.

4.7. $H_2O + CO$

For CO diluted in H_2O, only the 2ν ^{12}CO and 3ν ^{12}CO features were visible at 4260 and 6339 cm^{-1} respectively. Compared to a pure ice, each showed an increase in peak position (by 8 cm^{-1} and 1 cm^{-1}, respectively) and each broadened, by 30 cm^{-1} and 1 cm^{-1} respectively. Only the strength of the 2ν ^{12}CO feature was able to be determined from our data ($(1.4 \pm 0.1) \times 10^{-19}$ cm molecule^{-1}), and it was found to be comparable to the strength in the pure ice ($(1.6 \pm 0.1) \times 10^{-19}$ cm molecule^{-1}).

4.8. $H_2O + NH_3$

For the NH_3 diluted in H_2O, all observed features were seen to shift in peak position in comparison to pure NH_3, with increases ranging from $22 - 82$ cm^{-1}, and to decrease in FWHM by $55 - 97$ cm^{-1}. The strengths of all detectable features also decreased from their pure ice values by approximately 1.5 times. The strength of the $(\nu_1 + 2\nu_2 + \nu_4)$ mode near 6136 cm^{-1} could not be determined from our data.

$H_2O + NH_3$ (~3:1) at 9 K was studied by Moore et al. (2007). Their results included peak positions of the $(\nu_1 + \nu_2)$ and $(\nu_1 + \nu_4)$ vibrational modes. For the $(\nu_1 + \nu_2)$ feature, Moore et al. (2007) reported a peak position of 4478 cm^{-1}, which is further (by 7 cm^{-1}) from the pure ice value than our results indicate. The $(\nu_1 + \nu_4)$ mode also had a larger change from the pure ice value than seen in our results (by 2 cm^{-1}). Moore et al. (2007) did not calculate bands strengths.

5. Discussion and Implications

These experimental data can be used for more powerful interpretations of observations of astrophysical ices. In particular, the band strengths measured here may be used to more accurately determine column densities of ice components in the ISM. As shown in Gerakines et al. (2005), using our laboratory data, we can predict the optical depths of near-IR ice absorptions for several astrophysical objects. We have estimated the optical depths for several lines of sight in the ISM using the widths and strengths (as well as previously published column densities) for some of the near-IR features of our H_2O-dominated mixtures(e.g., Gerakines et al. 1999; Gibb et al. 2004). These estimates are listed in Table 4 and, due to their direct dependence on band strengths, show weakening in comparison to the results predicted in Gerakines et al. (2005). The estimates here are more appropriate to interstellar ices than our pure ices analysis in Gerakines et al. (2005), since interstellar ices are dominated by water ice. However they may not fully reflect the most realistic cases for these objects, as some are located in highly energetic environments, such as NGC 7538 IRS 9, GL 7009S, and GL 2136, which are all in the vicinity of young stellar objects (YSOs) and therefore undergoing various degrees of heating and/or energetic processing (Gibb et al. 2000).

N_2-dominated ice spectra may be used in comparison with observed planetary ices instead of pure ices to deduce information about the general composition of the surface ice. An example is Fig. 2 in Quirico et al. (1999) in which the spectrum of Triton is compared with laboratory transmission spectrum of pure ices CH_4, CO, N_2, CO_2, and H_2O. Similar to Triton, Pluto has been recently investigated by Buie et al. (2010) and has shown signs of N_2 ice, however, the behavior (i.e. seasonal effects) of ices on both planetary surfaces remains poorly understood. With the upcoming New Horizons mission in 2015, the data presented here may be useful for interpretation and further understanding of the general composition of the planetary surface. However, the chemical compositions of icy planetary bodies are affected by particle radiation or high-energy photons, resulting in the synthesis of new molecular species which can then be ejected into the gas phase by various mechanisms (Bringa & Johnson 2004). Studying the effect of UV radiolysis on these ices in addition to placing them in molecular mixture would lead to more realistic choices for comparison to observational data.

6. Summary and Future Work

In this paper, we have collected spectra of N_2 mixed with CO, CO_2, CH_4, and NH_3 in 5:1 ratios and of H_2O mixed with CO, CO_2, CH_4, and NH_3 in 5:1 ratios in the Near-IR region from 10,000-3,500 cm^{-1}(1.0-2.9 μm) and the mid-IR region from 4500-400 cm^{-1}

(2.2-25 μm) during the slow growth of films at $\sim$5 K and have used these to the determine near-IR band strengths listed in Table 2 and in Table 3. Future work will analyze the effect of UV radiolysis on both the pure ices previously discussed in Gerakines et al. (2005) and the ice mixtures described in this paper. We will also investigate the effects, if any, of ice composition on the near-IR band strengths as well as the differences between the near-IR band strengths of crystalline and amorphous ices.

7. Acknowledgments

C.R.R. gratefully acknowledges support for this research from the National Aeronautics and Space Administration under Grant No. NNG05GG95G issued through the Outer Planets Research Program and the Graduate Assistance in Areas of National Need (GAANN) Fellowship (US Dept of Education Grant No. P200A090143), as well as in earlier years through the NASA Alabama Space Grant Consortium Fellowship through Grant No. NNG05GE80H.

REFERENCES

Barucci, M. A., Cruikshank, D. P., Dotto, E., Merlin, F., Poulet, F., Dalle Ore, C., Fornasier, S., & de Bergh, C., 2005, A&A, 439, L1

Bernstein, M. P., Cruikshank, D. P., & Sandford, S. A., 2005, Icarus, 179, 527

Bernstein, M. P., Cruikshank, D. P., & Sandford, S. A., 2006, Icarus, 181, 302

Boogert, A. C. A., Schutte, W. A., Tielens, A. G. G. M., Whittet, D. C. B., Helmich, F. P., Ehrenfreund, P., Wesselius, P. R., de Graauw, Th., & Prusti, T., 1996, A&A, 315, L377

Boogert, A. C. A., Schutte, W. A., Helmich, F. P. Tielens, A. G. G. M., & Wooden, D. H., 1997, A&A, 317, 929

Bringa, E. M. & Johnson, R. E., 2004, ApJ, 603, 159

Brown, M. E., 2006, BAAS, 38, 550

Brown, M. E., 2008, in The Solar System Beyond Neptune, M. A. Barucci, H. Boehnhardt, D. P. Cruikshank, & R. Dotson (University of Arizona Press), 335

Brunetto, R., Caniglia, G., Baratta, G. A., & Palumbo, M. E., 2008, ApJ, 686, 1480

Buie, M. W. & Grundy, W. M., 2000, Icarus, 148, 324

Buie, M. W., Grundy, W. M., Young, E F., Young, L. A., & Stern, S. A., 2010, AJ, 139, 1128

Calvani, P., Cunsolo, S., Lupi, S., & Nucara, A., 1992, J. Chem. Phys., 96, 7372

Chiar, J. E., Adamson, J., Kerr, T. H., & Whittet, D. C. B., 1995, ApJ, 455, 234

Clark, R. N., Curchin, J. M., Jaumann, R., Cruikshank, D. P., Brown, R. H., Hoefen, T. M., Stephan, K., Moore, J. M., Buratti, B. J., Baines, K. H., Nicholson, P. D., & Nelson, R. M., 2008, Icarus, 193, 372

Cruikshank, D. P., 2007, LPI Contributions, 1357, 34

Cruikshank, D. P., Roush, T. L., Bartholomew, M. J., Geballe, T. R., Pendleton, Y. J., White, S. M., Bell, J. F., Davies, J. K., Owen, T. C., de Bergh, C., Tholen, D. J., Bernstein, M. P., Brown, R. H., Tryka, K. A., & Dalle Ore, C. M., 1998, Icarus, 135, 389

d'Hendecourt, L. B., & Allamandola, L. J., 1986, A&A, 64, 453

Filacchione, G., Capaccioni, F., Tosi, F., Coradini, A., Cerroni, P., Adriani, A., McCord, T. B., Baines, K. H., Bellucci, G., Brown, R. H., Bibring, J., Buratti, B. J., Clark, R. N., Combes, M., Cruikshank, D. P., Formisano, V., Jaumann, R., Langevin, Y. G., Matson, D. L., Mennella, V., Nelson, R. M., Nicholson, P. D., Sicardy, B., & Sotin, C., 2007, AGU Fall Meetings Abstract, B8

Gálvez, Ó., Maté, B., Herrero, V. J., & Escribano, R., 2009, ApJ, 703, 2101

Gerakines, P. A., Schutte, W. A., Greenberg, J. M., & van Dishoeck, E. F., 1995, A&A, 296, 810

Gerakines, P. A., Whittet, D. C. B., Ehrenfreund, P., Boogert, A. C. A., Tielens, A. G. G. M., Schutte, W. A., Chiar, J. E., van Dishoeck, E. F., Prusti, T., Helmich, F. P., & de Graauw, T., 1999, ApJ, 522, 357

Gerakines, P. A., Bray, J. J., Davis, A., & Richey, C. R., 2005, ApJ, 620, 1140

Gibb, E. L., Whittet, D. C. B., Schutte, W. A., Boogert, A. C. A., Chiar, J. E., Ehrenfreund, P., Gerakines, P. A., Keane, J. V., Tielens, A. G. G. M., van Dishoeck, E. F., & Kerkhof, O., 2000, ApJ, 536, 347

Gibb, E. L., Mumma, M. J., dello Russo, N., Disanti, M. A., & Magee-Sauer, K., 2003, Icarus, 165, 391

Gibb, E. L., Whittet, D. C. B., Boogert, A. C. A., & Tielens, A. G. G. M., 2004, ApJS, 151, 35

Grundy, W. M., Young, L. A., & Young, E. F., 2003, Icarus, 162, 222

Hansen, G. B. & McCord, T. B., 2008, Geophys. Res. Lett., 35, 1202

Hibbitts, C. A., McCord, T. B., & Hansen, G. B., 2000, J. Geophys. Res., 105, 22541

Hibbitts, C. A., Pappalardo, R. T., Hansen, G. B., & McCord, T. B., 2003, J. Geophys. Res., 108, 5036

Hudgins, D. M., Sandford, S. A., Allamandola, L. J., & Tielens, A. G. G. M., 1993, ApJS, 86, 713

Hudson, R. L., & Moore, M. H., 2001, J. Geophys. Res., 106, 33275

Jewitt, D. C., & Luu, J., 2004, Nature, 432, 731

Kerkhof, O., Schutte, W. A., &— Ehrenfreund, P., 1999, A&A, 346, 990

Lopes, R. M., Wall, S. D., Stofan, E. R., Wood, C. A., Nelson, R. M., Mitchell, K. L., Radebaugh, J., Stiles, B. W., Kamp, L. W., Lorenz, R. D., Lunine, J. I., Janssen, M. A., Farr, T. G., Mitri, G., Kirk, R., & Paganelli, F., 2008, AGU Fall Meetings Abstracts, A3

McCord, T. B., Hansen, G. B., Clark, R. N., Martin, P. D., Hibbitts, C. A., Fanale, F. P., Granahan, J. C., Segura, M., Matson, D. L., Johnson, T. V., Carlson, R. W., Smythe, W. D., & Danielson, G. E., 1998, J. Geophys. Res., 103, 8603

Moore, M. H., Ferrante, R. F., Hudson, R. L., & Stone, J. N., 2007, Icarus, 190, 260

Murakawa, K. and Tamura, M. and Nagata, T., 2000, ApJS, 128, 603

Oliveira, J. M., van Loon, J. T., Chen, C.-H. R., Tielens, A. G. G. M., Sloan, G. C. and Woods, P. M., Kemper, F., Indebetouw, R., Gordon, K. D., Boyer, M. L., Shiao, B., Madden, S., Speck, A. K., Meixner, M., & Marengo, M., 2009, ApJ, 707, 1269

Quirico, E., Doute, S., Schmitt, B., de Bergh, C., Cruikshank, D. P., Owen, T. C., Geballe, T. R., & Roush, T. L., 1999, Icarus, 139, 159

Quirico, E. and Schmitt, B., 1997, Icarus, 127, 354

Rauscher, B. J., Figer, D. F., Hill, R. J., Jakobsen, P. J., Moseley, S. H., Regan, M. W., & Strada, P., 2004, AAS Meeting, 204

Roush, T. L., 2001, J. Geophys. Res., 106, 33315

Schaller, E. L., & Brown, M. E., 2007, ApJ, 659, L61

Stansberry, J. A., 2004, in Icy Worlds of the Solar System, P. Dasch (Cambridge University Press), 139

Taban, I. M., Schutte, W. A., Pontoppidan, K. M., & van Dishoeck, E. F., 2003, A&A, 399, 169

Tielens, A. G. G. M, Tokunaga, A. T., Geballe, T. R., & Baas, F., 1991, ApJ, 381, 181

Trujillo, C. A., Brown, M. E., Rabinowitz, D. L., & Geballe, T. R., 2005, ApJ, 627, 1057

Vacca, W. D. and Cushing, M. C. and Simon, T., 2004, ApJ, 609, L29

Table 1. Mid-Infrared Features and Band Strengths Used in Strength Determinations

Molecule	$\tilde{\nu}$ [cm^{-1}]	λ [μm]	A [cm molecule^{-1}]	Reference
Pure CH_4	1306	7.657	7.0×10^{-18}	1
	2815	3.552	2.8×10^{-19}	2
CH_4 in H_2O+ CH_4 (1.03:1)	1302	7.680	8.1×10^{-18}	3
N_2+ CH_4 (10:1)	2820	3.546	3.4×10^{-19}	2
Pure CO_2 [a]	2283	6.639	7.8×10^{-17}	4
	3708	2.697	1.4×10^{-18}	4
CO_2 in H_2O+ CO_2 (1.6:1)	2279	6.639	7.6×10^{-17}	4
Pure CO [a]	2092	4.780	1.5×10^{-19} [b]	5
CO in H_2O+ CO (2.1:1)	2092	4.780	1.2×10^{-19} [b]	4
Pure NH_3 [a]	1070	9.346	1.2×10^{-17}	5
NH_3 in H_2O+ NH_3 (11:1)	1070	9.346	1.3×10^{-17}	3

[a]Used for N_2 mixture. See text for further discussion.

[b]Although this is a feature of ^{13}CO, its band strength is expressed in units of cm per ^{12}CO molecule.

Note. — (1) Boogert et al. (1997); (2) Brunetto et al. (2008); (3) Kerkhof et al. (1999); (4) Gerakines et al. (1995); (5) d'Hendecourt & Allamandola (1986).

Table 2. Observed Near-IR Features and Band Strengths of N_2-dominated Ice Mixtures at 5 K

Peak Position $\tilde{\nu}$ [cm^{-1}]	Peak Position λ [μm]	FWHM, $\Delta\tilde{\nu}$ [cm^{-1}]	Vibration Mode	Relative Growth [a] Rate	Strength, A [cm molecule^{-1}]
N_2+CH_4 (5:1)					
4125	2.425	14	$\nu_2 + 2\nu_4$	$(3.9 \pm 0.3) \times 10^{-2}$	$(1.3 \pm 0.1) \times 10^{-20}$
4222	2.374	11	$\nu_1 + \nu_4$	$(79 \pm 4) \times 10^{-2}$	$(2.7 \pm 0.1) \times 10^{-19}$
4311	2.320	18	$\nu_3 + \nu_4$	$(230 \pm 4) \times 10^{-2}$	$(7.9 \pm 0.1) \times 10^{-19}$
4539	2.203	15	$\nu_2 + \nu_3$	$(27 \pm 0.4) \times 10^{-2}$	$(9.2 \pm 0.1) \times 10^{-20}$
5576	1.793	15	$\nu_3 + 2\nu_4$	$(3.6 \pm 0.4) \times 10^{-2}$	$(1.2 \pm 0.1) \times 10^{-20}$
5811	1.721	15	$\nu_2 + \nu_3 + \nu_4$	$(7.1 \pm 0.4) \times 10^{-2}$	$(2.4 \pm 0.1) \times 10^{-20}$
6000	1.667	18	$2\nu_3$	$(11 \pm 0.4) \times 10^{-2}$	$(3.6 \pm 0.1) \times 10^{-20}$
7503	1.333	18	$\nu_2 + 2\nu_3$	$(20 \pm 0.4) \times 10^{-3}$	$(6.8 \pm 0.1) \times 10^{-21}$
8422	1.187	26	$[\nu_1] + [\nu_1] + [\nu_4] + [\nu_4]$	...	...
8611	1.161	35	$2\nu_3 + 2\nu_4$	$(5.4 \pm 0.4) \times 10^{-2}$	$(1.8 \pm 0.1) \times 10^{-20}$
N_2+CO_2 (5:1)					
4840	2.066	7	$4\nu_2 + \nu_3$	$(9.3 \pm 0.7) \times 10^{-3}$	$(1.3 \pm 0.1) \times 10^{-20}$
4975	2.010	7	$\nu_1 + 2\nu_2 + \nu_3$	$(59 \pm 0.7) \times 10^{-3}$	$(8.2 \pm 0.1) \times 10^{-20}$
5090	1.965	7	$2\nu_1 + \nu_3$	$(25 \pm 0.7) \times 10^{-3}$	$(3.5 \pm 0.1) \times 10^{-20}$
6218	1.608	8	$\nu_1 + 4\nu_2 + \nu_3$	...	...
6340	1.577	9	$2\nu_1 + 2\nu_2 + \nu_3$	...	...
6970	1.435	10	$3\nu_3$	...	...
9955	1.005	6	$4\nu_3 + \nu_2$(?)	...	...
N_2+CO (5:1)					
4159	2.404	7	2ν ^{13}CO	...	...
4253	2.351	6	2ν ^{12}CO	$(73 \pm 7) \times 10^{-2}$	$(1.1 \pm 0.1) \times 10^{-19}$
6339	1.578	9	3ν ^{12}CO	...	...
8505	1.176	9	?	...	...
N_2+NH_3 (5:1)					
4444	2.250	22	$\nu_1 + \nu_2$ (?)	$(18 \pm 0.8) \times 10^{-3}$	$(2.2 \pm 0.1) \times 10^{-19}$
5042	1.983	13	$\nu_1 + \nu_4$ (?)	$(33 \pm 0.8) \times 10^{-3}$	$(4.0 \pm 0.1) \times 10^{-19}$
6034	1.657	-	$\nu_1 + \nu_2 + \nu_4$ (?)	...	...
6598	1.516	21	$2\nu_1$ (?)	$(7.2 \pm 0.2) \times 10^{-3}$	$(8.6 \pm 0.2) \times 10^{-20}$

[a]The slope of the linear trend in the near-IR vs. mid-IR band areas shown in Figures 3-6.

Note. — Vibrational mode assignments, except those in NH_3 mixtures, from Calvani et al. 1992 and Quirico & Schmitt 1997; NH_3 assignments are uncertain, however, are similar to those made in Moore et al. (2007).

Table 3. Observed Near-IR Features and Band Strengths in H_2O-dominated Ice Mixtures at 5 K

Peak Position		FWHM, $\Delta\tilde{\nu}$	Vibration	Relative Growth [a]	Strength, A
$\tilde{\nu}$ [cm^{-1}]	λ [μm]	[cm^{-1}]	Mode	Rate	[cm molecule^{-1}]
H_2O+CH_4 (5:1)					
4209	2.376	17	$\nu_1 + \nu_4$	$(3.6 \pm 0.1) \times 10^{-2}$	$(2.9 \pm 0.1) \times 10^{-19}$
4308	2.321	16	$\nu_3 + \nu_4$	$(7.0 \pm 0.3) \times 10^{-2}$	$(5.7 \pm 0.2) \times 10^{-19}$
4528	2.208	10	$\nu_2 + \nu_3$	...	...
5640	1.773	8	$\nu_3 + 2\nu_4$	...	...
5804	1.723	23	$\nu_2 + \nu_3 + \nu_4$	...	...
5995	1.668	11	$2\nu_3$	...	...
7700	1.299	26	$\nu_2 + 2\nu_3$	...	...
8569	1.167	22	$[\nu_1] + [\nu_3] + [\nu_4] + [\nu_4]$	...	...
8612	1.161	7	$2\nu_3 + 2\nu_4$	...	...
8962	1.116	36	$\nu_2 + 2\nu_3 + \nu_4$	...	...
9039	1.106	22	$3\nu_3$	...	...
H_2O+CO_2 (5:1)					
4965	2.014	9	$\nu_1 + 2\nu_2 + \nu_3$	$(3.1 \pm 0.1) \times 10^{-3}$	$(2.3 \pm 0.1) \times 10^{-19}$
5086	1.966	10	$2\nu_1 + \nu_3$	$(10 \pm 0.5) \times 10^{-4}$	$(7.6 \pm 0.4) \times 10^{-20}$
6051	1.653	100	$\nu_1 + 4\nu_2 + \nu_3$	...	...
6325	1.581	78	$2\nu_1 + 2\nu_2 + \nu_3$	...	...
6864	1.457	179	$3\nu_3$	...	...
H_2O+CO (5:1)					
4260	2.347	33	2ν ^{12}CO	1.2 ± 0.7	$(1.4 \pm 0.8) \times 10^{-19}$
6339	1.575	5	3ν ^{12}CO	...	...
H_2O+NH_3 (5:1)					
4518	2.213	22	$\nu_1 + \nu_2$ (?)	$(44 \pm 0.8) \times 10^{-3}$	$(5.7 \pm 0.1) \times 10^{-19}$
5015	1.994	13	$\nu_1 + \nu_4$ (?)	$(38 \pm 0.8) \times 10^{-3}$	$(4.9 \pm 0.1) \times 10^{-19}$
6136	1.630	-	$\nu_1 + \nu_2 + \nu_4$ (?)	...	...
6597	1.516	21	$2\nu_1$ (?)	$(27 \pm 0.8) \times 10^{-4}$	$(3.9 \pm 0.1) \times 10^{-20}$

[a]The slope of the linear trend in the near-IR vs. mid-IR band areas shown in Figures 7-10.

Note. — Vibrational mode assignments, except those in NH_3 mixtures, from Calvani et al. 1992 and Quirico & Schmitt 1997; NH_3 assignments are uncertain, however, are similar to those made in Moore et al. (2007).

Table 4. Column Densities[a] and Predicted Near-IR Optical Depths[b] of Interstellar Ices Diluted in H_2O

	W33A	NGC 7538 IRS9	Elias 16	Sgr A*	GL 7009S	GL 2136
CH_4						
N	1.7×10^{17}	1.5×10^{17}	—	2.6×10^{16}	4.8×10^{17}	—
$\tau(2.376\,\mu m)$	0.003	0.002	—	< 0.001	0.008	—
$\tau(2.321\,\mu m)$	0.006	0.006	—	< 0.001	0.01	—
CO_2						
N	1.4×10^{18}	1.7×10^{18}	4.5×10^{17}	1.8×10^{17}	2.5×10^{18}	8.0×10^{17}
$\tau(2.014\,\mu m)$	0.04	0.05	0.01	0.005	0.07	0.02
$\tau(1.966\,\mu m)$	0.01	0.01	0.004	.001	0.02	0.006
CO						
N	8.8×10^{17}	1.2×10^{18}	6.3×10^{17}	$< 2 \times 10^{17}$	1.8×10^{18}	1.0×10^{17}
$\tau(2.347\,\mu m)$	0.004	0.005	0.002	<0.001	0.008	<0.001
NH_3						
N	1.7×10^{18}	9.8×10^{17}	$\lesssim 2.3 \times 10^{17}$	$2.6 - 3.9 \times 10^{17}$	—	—
$\tau(2.213\ \mu m)$	0.04	0.02	$\lesssim 0.006$	$0.006 - 0.01$	—	—
$\tau(1.994\ \mu m)$	0.06	0.03	$\lesssim 0.009$	$0.01 - 0.02$	—	—

[a]Column densities (N) have units of cm^{-2}; Gibb et al. (2004).

[b]Optical depths have been calculated from the listed column densities, using width and strength data listed in Table 3.

Fig. 1.— Combined near- and mid-IR spectra (10,000-400 cm^{-1}, 1.0-25 μm) of ice films at $T \sim 5$ K for the N_2-dominated mixtures. The sinusoidal baseline behaviors (strongest in the $N_2 + CO_2$ and $N_2 + CO$ samples) are due to interference of the IR beam within the samples. Some features due to minor contamination by H_2O and CO_2 are also visible (see text for a full discussion).

Fig. 2.— Combined near- and mid-IR spectra (10,000-400 cm^{-1}, 1.0-25 μm) of ice films at $T \sim 5$ K for the H_2O-dominated mixtures. The sinusoidal baseline behaviors are due to interference of the IR beam within the samples. Some features due to minor contamination by CO_2 are also visible (see text for a full discussion).

Fig. 3.— Top: Selected near-IR absorbance spectra of a $N_2 + CH_4$ (5:1) ice mixture at $T \sim 5$ K for the most prominent features studied. Bottom: Integrated areas (in cm^{-1}) of CH_4 features vs. the area (in cm^{-1}) of the 2825 cm^{-1} (3.540 μm) feature during deposition at $T \sim 5$ K. The solid lines are linear fits to the solid symbols, and data points shown as empty symbols were omitted from the fits (see explanation in text).

Fig. 4.— Top: Selected near-IR absorbance spectrum of a $N_2 + CO_2$ (5:1) ice mixture at ~ 5 K for the most prominent features studied. Bottom: Integrated areas (in cm^{-1}) of CO_2 features vs. the area (in cm^{-1}) of the 3711 cm^{-1} (2.695 μm) feature during deposition at ~ 5 K. The solid lines are linear fits to the solid symbols, and data points shown as empty symbols were omitted from the fits (see explanation in text).

Fig. 5.— Top: Selected near-IR absorbance spectrum of a $N_2 + CO$ (5:1) ice mixture at ~ 5 K for the most prominent features studied. Bottom: Integrated areas (in cm^{-1}) of CO features vs. the area (in cm^{-1}) of the 2092 cm^{-1} (4.780 μm) feature during deposition at ~ 5 K. The solid lines are linear fits to the solid symbols.

Fig. 6.— Top: Selected near-IR absorbance spectra of a $N_2 + NH_3$ (5:1) ice mixture at ~ 5 K for the most prominent features studied. Bottom: Integrated areas (in cm^{-1}) of NH_3 features vs. the area (in cm^{-1}) of the 1146 cm^{-1} (8.726 μm) feature during deposition at ~ 5 K. The solid lines are linear fit to the solid symbols, and data points shown as empty symbols were omitted from the fits (see explanation in text).

Fig. 7.— Top: Selected near-IR absorbance spectrum of a $H_2O + CH_4$ (5:1) ice mixture at ~ 5 K for the prominent most features studied. Bottom: Integrated areas (in cm^{-1}) of CH_4 features vs. the area (in cm^{-1}) of the 1306 cm^{-1} (7.657 μm) feature during deposition at ~ 5 K. The solid lines are linear fits to the solid symbols.

Fig. 8.— Top: Selected near-IR absorbance spectrum of a H_2O + CO_2 (5:1) ice mixture at $\sim$ 5 K for the most prominent features studied. Bottom: Integrated areas (in cm^{-1}) of CO_2 features vs. the area (in cm^{-1}) of the 2280 cm^{-1} (4.386 μm) feature during deposition at $\sim$ 5 K. The solid lines are linear fits to the solid symbols, and data points shown as empty symbols were omitted from the fits (see explanation in text).

Fig. 9.— Top: Selected near-IR absorbance spectrum of a H_2O + CO (5:1) ice mixture at $\sim$ 5 K for the most prominent features studied. Bottom: Integrated areas (in cm^{-1}) of CO features vs. the area (in cm^{-1}) of the 2092 cm^{-1} (4.386 μm) feature during deposition at $\sim$ 5 K. The solid lines are linear fits to the solid symbols.

Fig. 10.— Top: Selected near-IR absorbance spectra of a H_2O + NH_3 (5:1) ice mixture at $\sim$ 5 K for the most prominent features studied. Bottom: Integrated areas (in cm^{-1}) of NH_3 features vs. the area (in cm^{-1}) of the 1110 cm^{-1} (9.009 μm) feature during deposition at $\sim$ 5 K. The solid lines are linear fits to the solid symbols, and data points shown as empty symbols were omitted from the fits (see explanation in text).

FIGURE 1

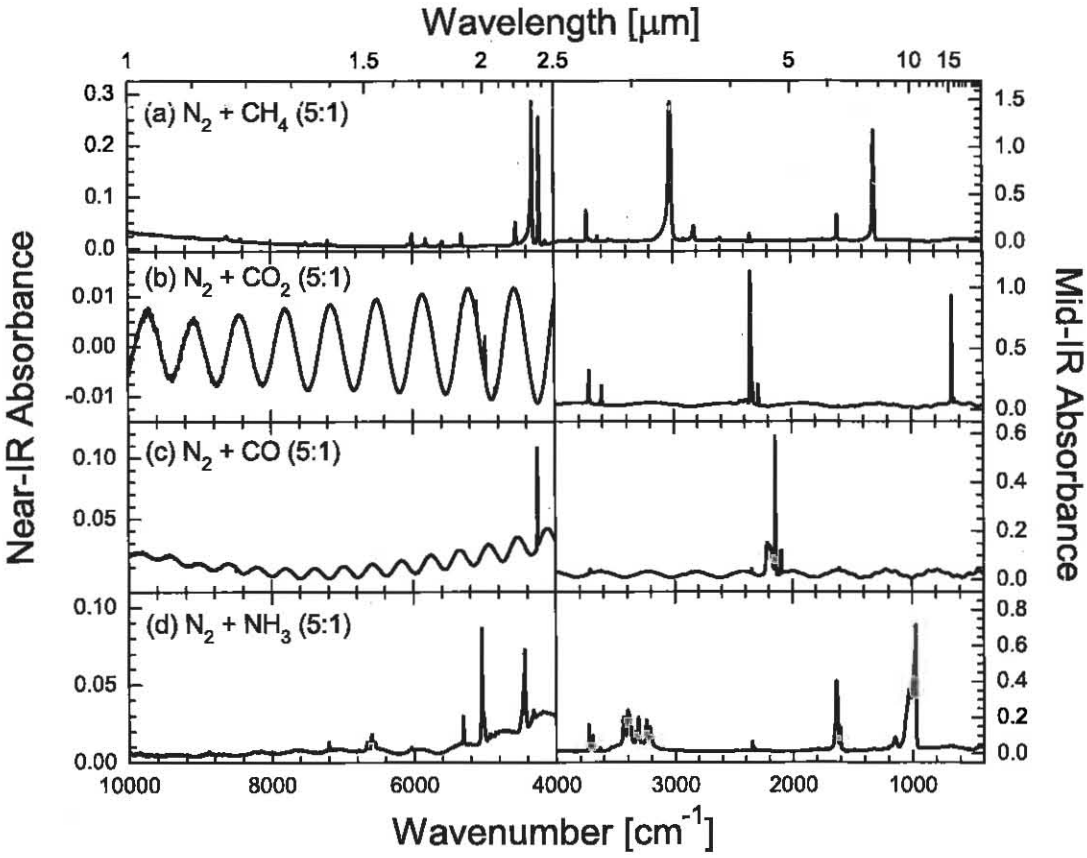
Wavelength [μm]
1
1.5
2
2.5
5
10
15
(a) N2 + CH4 (5:1)
(b) N2 + CO2 (5:1)
(c) N2 + CO (5:1)
(d) N2 + NH3 (5:1)
Near-IR Absorbance
Mid-IR Absorbance
Wavenumber [cm-1]
10000
8000
6000
4000
3000
2000
1000

FIGURE 2

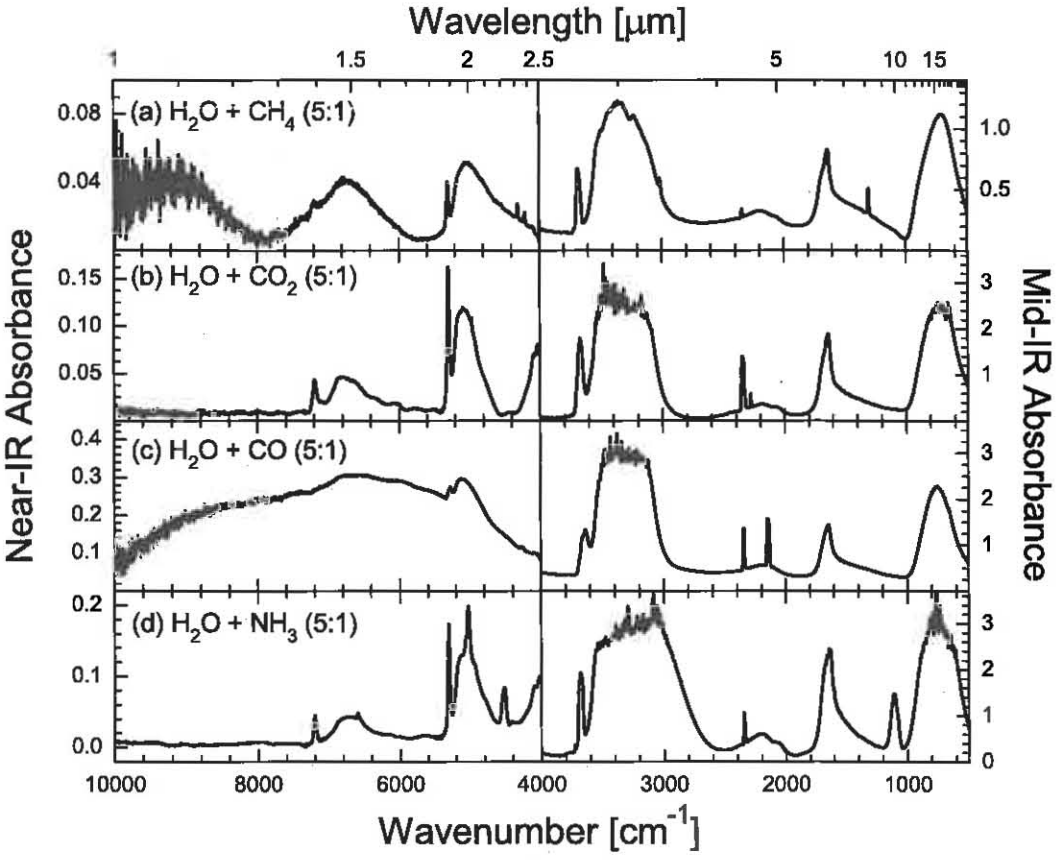
Wavelength [μm]
1
1.5
2
2.5
5
10
15
(a) H2O + CH4 (5:1)
(b) H2O + CO2 (5:1)
(c) H2O + CO (5:1)
(d) H2O + NH3 (5:1)
Near-IR Absorbance
Mid-IR Absorbance
Wavenumber [cm-1]
10000
8000
6000
4000
3000
2000
1000

FIGURE 3

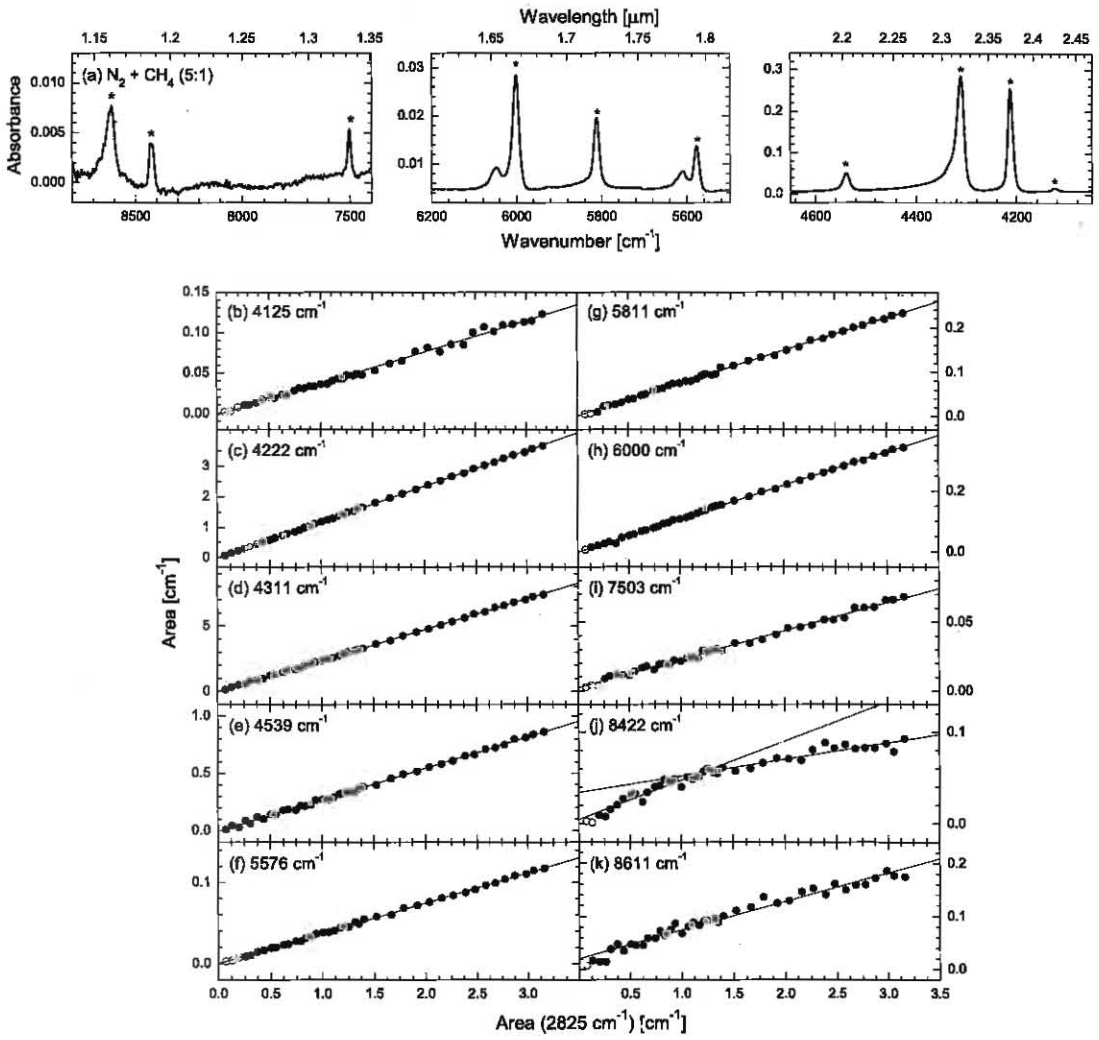
Wavelength [μm]
Absorbance
(a) N2 + CH4 (5:1)
Wavenumber [cm-1]
(b) 4125 cm-1
(c) 4222 cm-1
(d) 4311 cm-1
(e) 4539 cm-1
(f) 5576 cm-1
(g) 5811 cm-1
(h) 6000 cm-1
(i) 7503 cm-1
(j) 8422 cm-1
(k) 8611 cm-1
Area [cm-1]
Area (2825 cm-1) [cm-1]

FIGURE 4

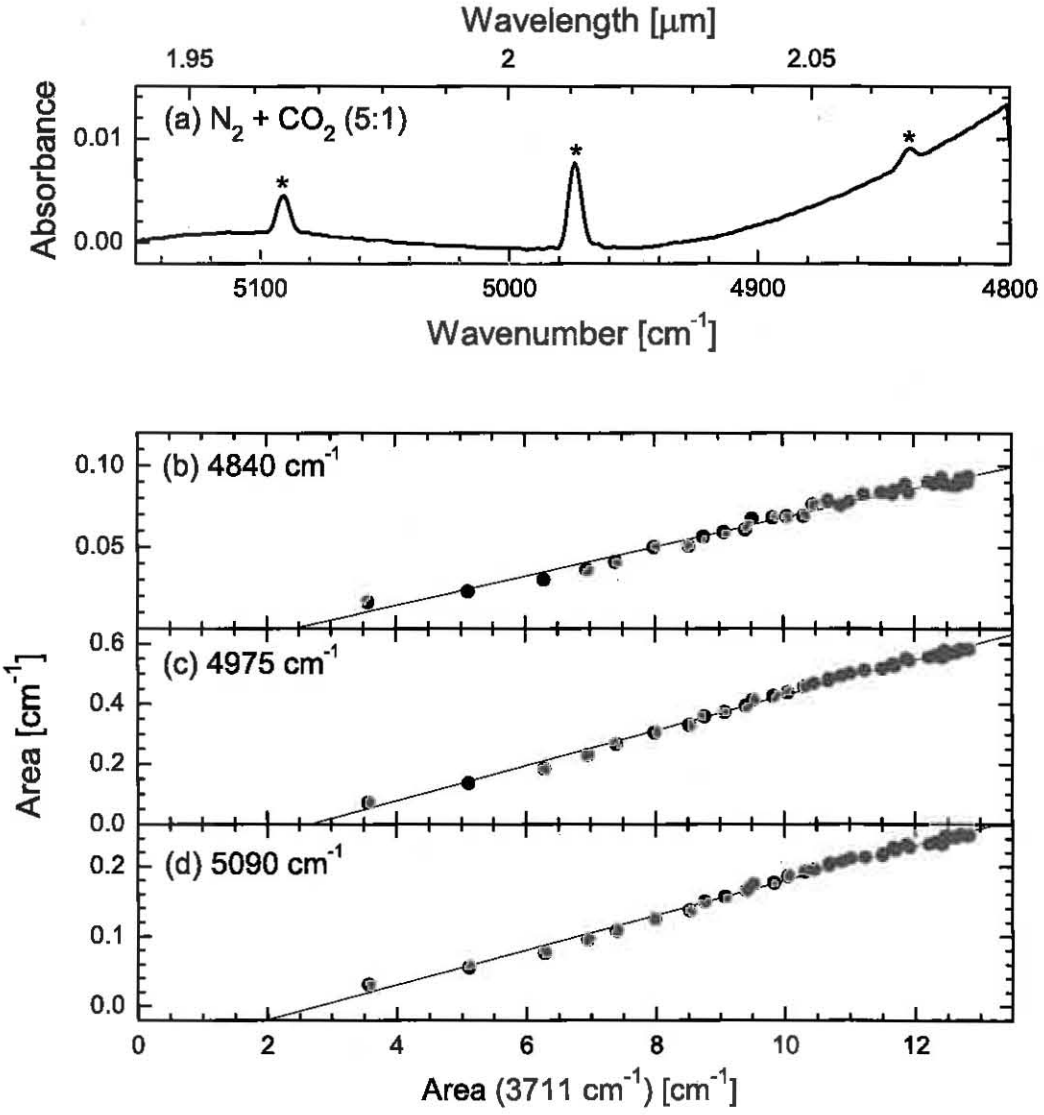
Wavelength [μm]
1.95
2
2.05
Absorbance
0.01
0.00
(a) N2 + CO2 (5:1)
*
*
*
5100
5000
4900
4800
Wavenumber [cm-1]
0.10
0.05
(b) 4840 cm-1
0.6
0.4
0.2
0.0
(c) 4975 cm-1
0.2
0.1
0.0
(d) 5090 cm-1
Area [cm-1]
0
2
4
6
8
10
12
Area (3711 cm-1) [cm-1]

FIGURE 5

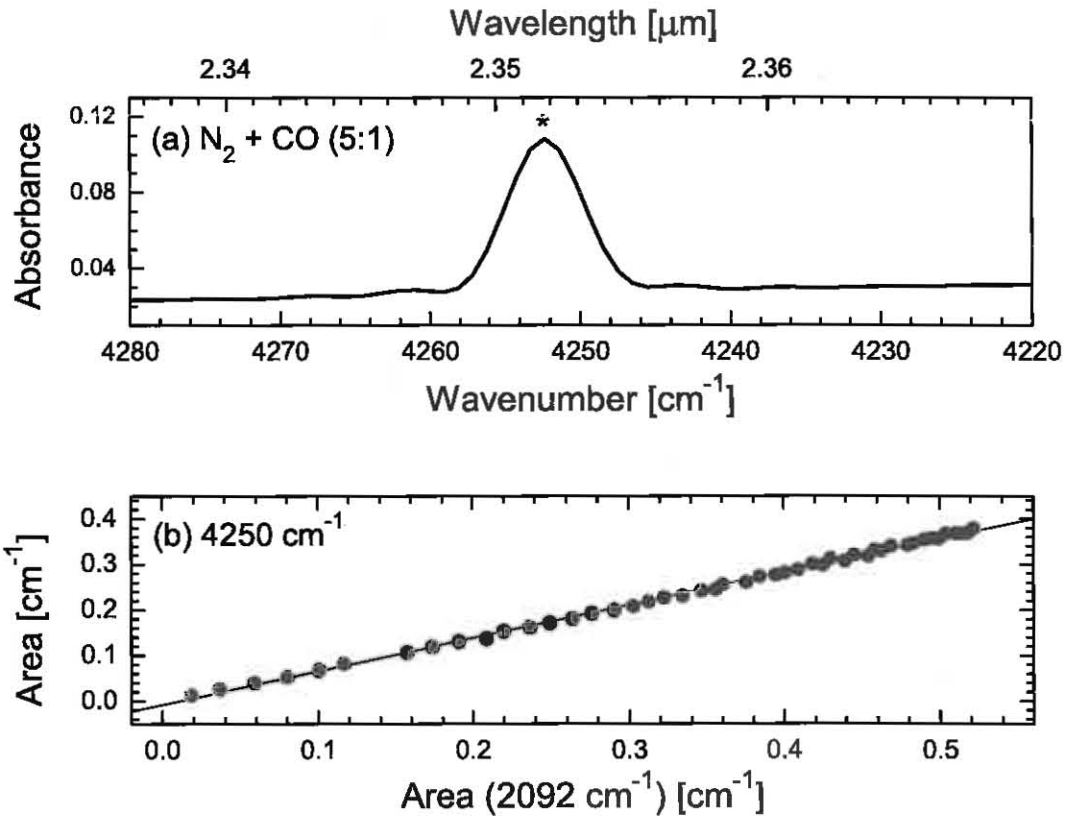
Wavelength [μm]
2.34
2.35
2.36
0.12
0.08
0.04
Absorbance
(a) N2 + CO (5:1)
*
4280
4270
4260
4250
4240
4230
4220
Wavenumber [cm-1]
0.4
0.3
0.2
0.1
0.0
Area [cm-1]
(b) 4250 cm-1
0.0
0.1
0.2
0.3
0.4
0.5
Area (2092 cm-1) [cm-1]

FIGURE 6

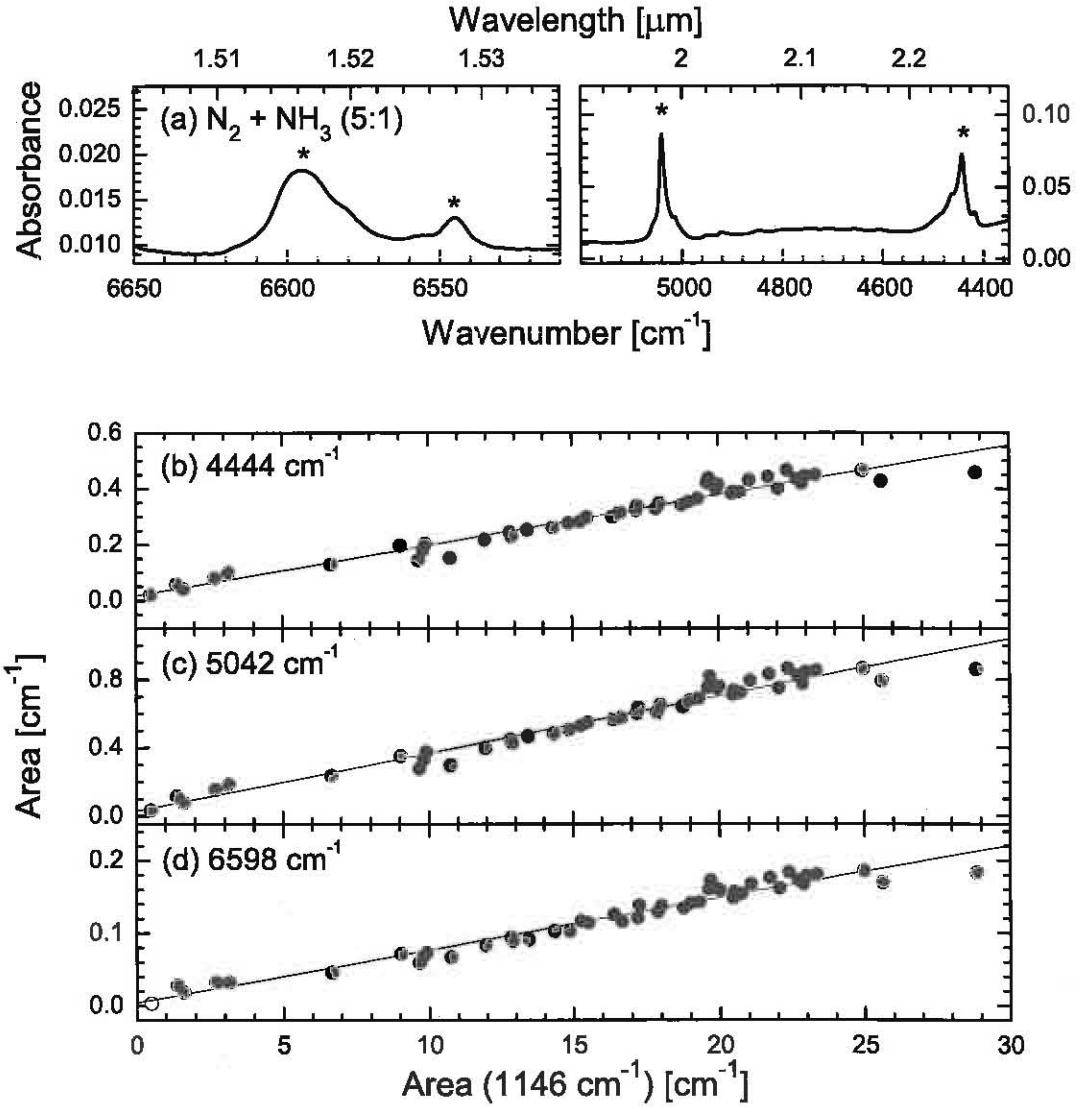
Wavelength [μm]
1.51
1.52
1.53
2
2.1
2.2
Absorbance
(a) N2 + NH3 (5:1)
0.025
0.020
0.015
0.010
0.10
0.05
0.00
6650
6600
6550
5000
4800
4600
4400
Wavenumber [cm-1]
(b) 4444 cm-1
(c) 5042 cm-1
(d) 6598 cm-1
Area [cm-1]
0.6
0.4
0.2
0.0
0.8
0.1
0
5
10
15
20
25
30
Area (1146 cm-1) [cm-1]

FIGURE 7

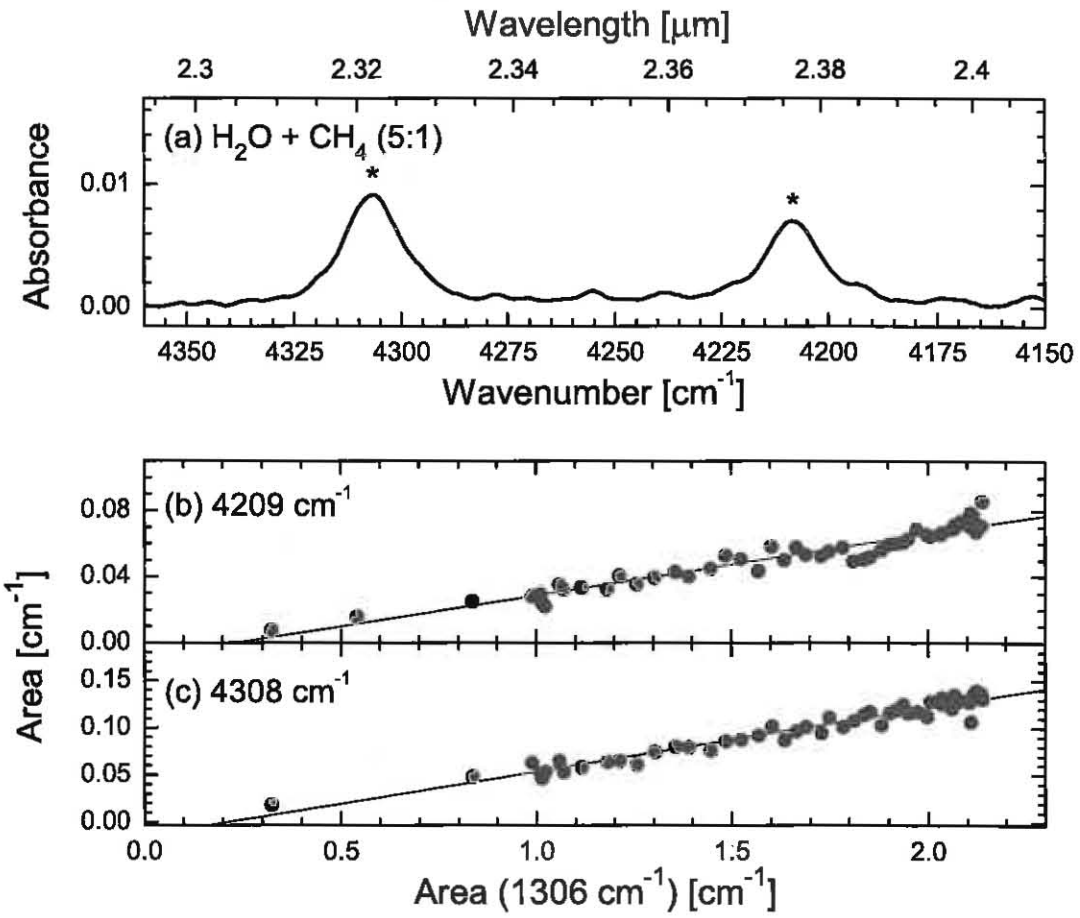
Wavelength [μm]
2.3
2.32
2.34
2.36
2.38
2.4
(a) H_2O + CH_4 (5:1)
Absorbance
0.01
0.00
4350
4325
4300
4275
4250
4225
4200
4175
4150
Wavenumber [cm^{-1}]
(b) 4209 cm^{-1}
0.08
0.04
0.00
(c) 4308 cm^{-1}
0.15
0.10
0.05
0.00
Area [cm^{-1}]
0.0
0.5
1.0
1.5
2.0
Area (1306 cm^{-1}) [cm^{-1}]

FIGURE 8

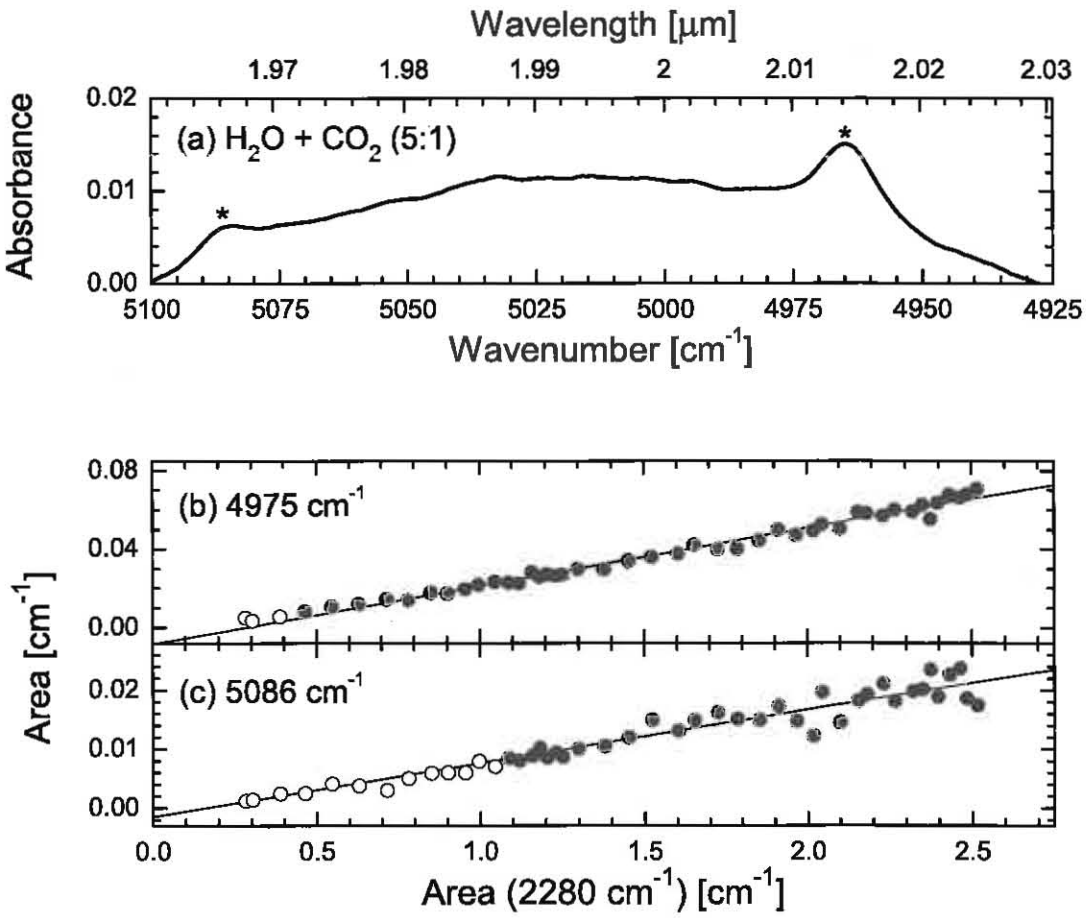
Wavelength [μm]
1.97
1.98
1.99
2
2.01
2.02
2.03
Absorbance
0.02
0.01
0.00
(a) H2O + CO2 (5:1)
*
*
5100
5075
5050
5025
5000
4975
4950
4925
Wavenumber [cm-1]
0.08
0.04
0.00
(b) 4975 cm-1
0.02
0.01
0.00
(c) 5086 cm-1
Area [cm-1]
0.0
0.5
1.0
1.5
2.0
2.5
Area (2280 cm-1) [cm-1]

FIGURE 9

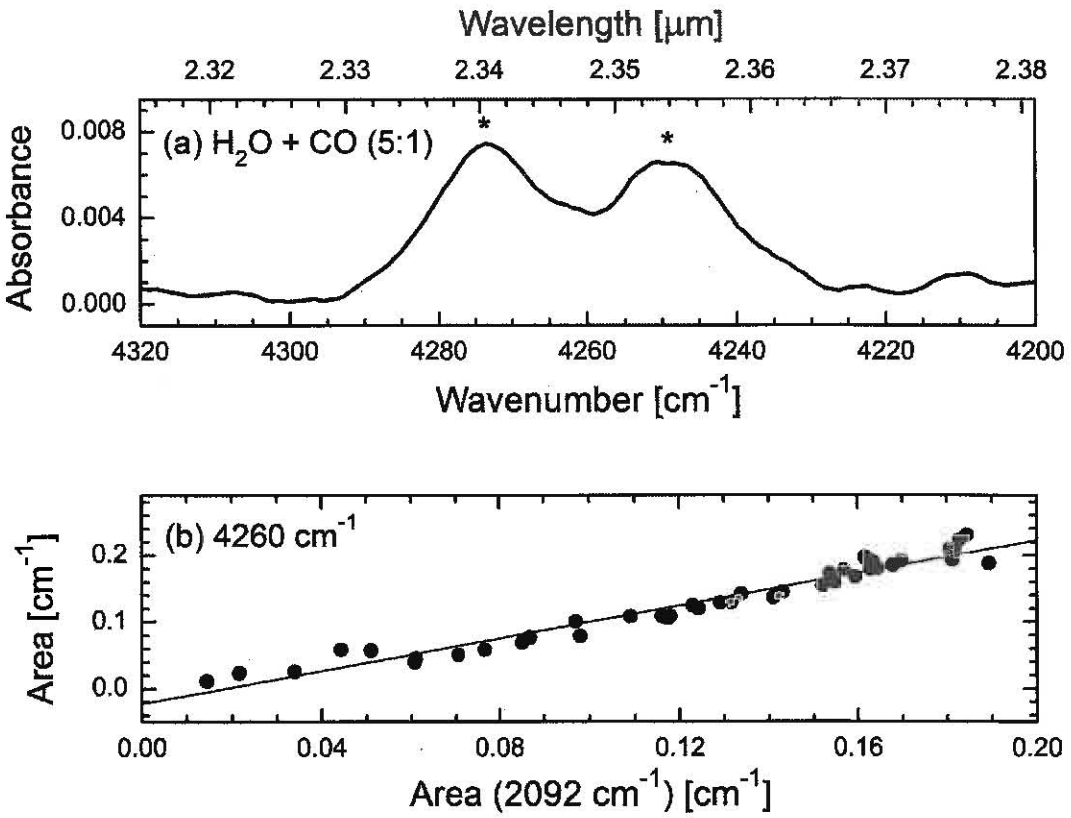
Wavelength [μm]
2.32
2.33
2.34
2.35
2.36
2.37
2.38
Absorbance
0.008
0.004
0.000
(a) H2O + CO (5:1)
*
*
4320
4300
4280
4260
4240
4220
4200
Wavenumber [cm-1]
Area [cm-1]
0.2
0.1
0.0
(b) 4260 cm-1
0.00
0.04
0.08
0.12
0.16
0.20
Area (2092 cm-1) [cm-1]

FIGURE 10

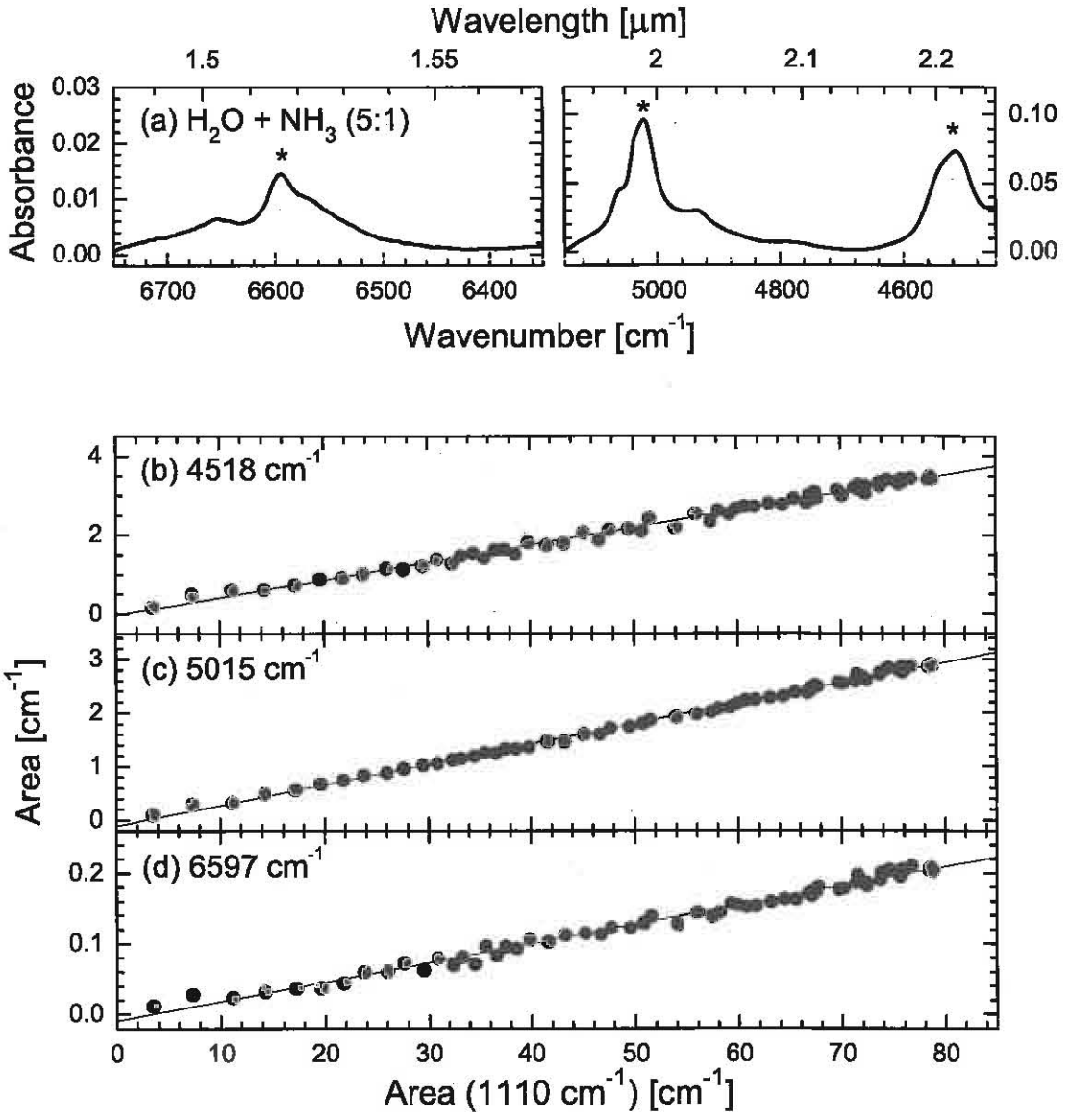
Wavelength [μm]
1.5
1.55
2
2.1
2.2
Absorbance
0.03
0.02
0.01
0.00
(a) H2O + NH3 (5:1)
*
*
*
0.10
0.05
0.00
6700
6600
6500
6400
5000
4800
4600
Wavenumber [cm-1]
Area [cm-1]
4
2
0
(b) 4518 cm-1
3
2
1
0
(c) 5015 cm-1
0.2
0.1
0.0
(d) 6597 cm-1
0
10
20
30
40
50
60
70
80
Area (1110 cm-1) [cm-1]